J. Nonlinear Sci. Vol. 7: pp. 281–314 (1997)

Journal of
Nonlinear
Science

Constrained Euler Buckling

G. Domokos[1], P. Holmes[2], and B. Royce[3]

[1] Department of Strength of Materials, Technical University of Budapest, H-1521 Budapest, Hungary

[2] Program in Applied and Computational Mathematics and Department of Mechanical and Aerospace Engineering, Princeton University, Princeton, NJ 08544, USA

[3] Department of Mechanical and Aerospace Engineering, and Princeton Materials Institute, Princeton University, Princeton, NJ 08544, USA

Received June 27, 1996; revised manuscript accepted for publication September 11, 1996
Communicated by Jerrold Marsden and Stephen Wiggins

Dedicated to the memory of Juan C. Simo[†]

Summary. We consider elastic buckling of an inextensible beam confined to the plane and subject to fixed end displacements, in the presence of rigid, frictionless side-walls which constrain overall lateral displacements. We formulate the geometrically nonlinear (Euler) problem, derive some analytical results for special cases, and develop a numerical shooting scheme for solution. We compare these theoretical and numerical results with experiments on slender steel beams. In contrast to the simple behavior of the unconstrained problem, we find a rich bifurcation structure, with multiple branches and concomitant hysteresis in the overall load-displacement curves.

Key words. Elastic buckling, bifurcation, nonlinear boundary value problem

MSC numbers. 34B15, 58F14, 73K05

1. Introduction

Buckling is important in applications as diverse as automotive crash protection and fiber preparation of nonwoven fabrics. The work described in this paper was motivated by the latter, specifically, a desire to understand plastic buckling of polypropylene fibers in a "stuffer box" process. In this manufacturing environment, many approximately parallel fibers forming a "tow" emerge from rapidly rotating rollers into a confined half-space in which they suffer large velocity changes as a result of collisions with previously slowed

[†] This paper was solicited by the editors to be part of a volume dedicated to the memory of Juan C. Simo.

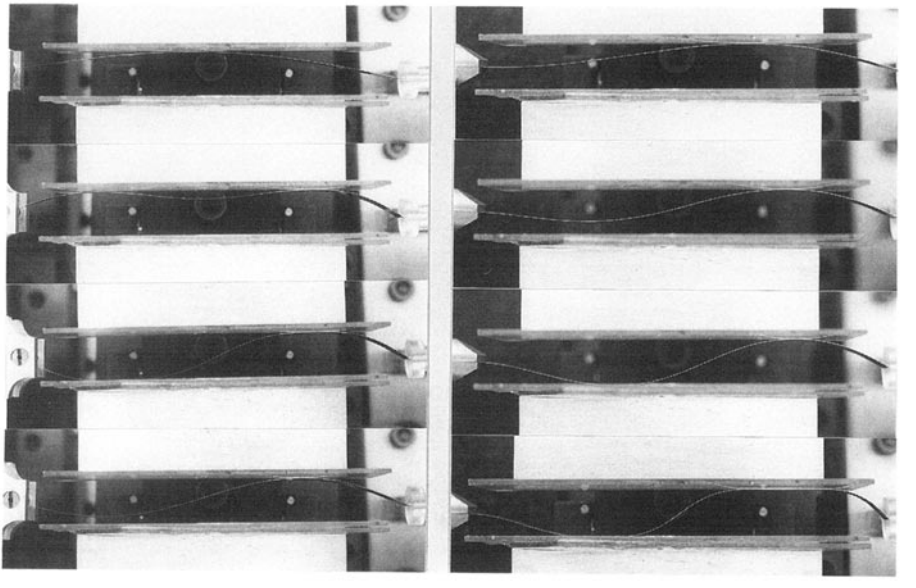

Fig. 1. Some typical buckled shapes. Left column: pinned-pinned beam; right column: clamped-pinned beam. See Section 4 for description of asymmetrical shapes.

and crimped material. At the rollers, the tow approximates a close-packed cylinder configuration, and during crimping the fibers are able to expand into a less close-packed form. The final configuration of the crimped tow suggests that cooperative deformation of many fibers occurs during this process. Our desire to better understand the basic mechanics has led us to consider a simpler, but still interesting problem more amenable to theoretical, numerical, and experimental study. In this paper, we address the planar *elastic* buckling of an inextensible lamella (beam) confined between rigid, parallel, frictionless walls. The specimen shape confines buckling to the plane normal to the lamella's major axis. Geometries more characteristic of the manufacturing process, with wedge-shaped and circular constraint walls, will be treated in future work. Here our main goal is to understand the basic mechanics of the process, including buckling mode selection and overall end load-displacement relations.

In a typical experiment of the type to be described in Section 4, the end positions of a slender steel lamella are constrained and their separation is gradually decreased, leading to buckling and contact with one or both side-walls. Point contact can become line contact as the end load increases; secondary buckling of the flattened portion and jumping between different modes may then ensue. Figure 1 shows two sequences of photographs taken during experimental runs, illustrating multiple contacts, mode jumping, and flattening of the beam against the constraint walls: all phenomena to be investigated below.

The model developed in Section 2 is based on the classical one of Euler [Eul44]. It is fully nonlinear geometrically [Ant95] but employs a linear constitutive relation, adequate for the slender lamellae and modest forces and moments used in our experimental work.

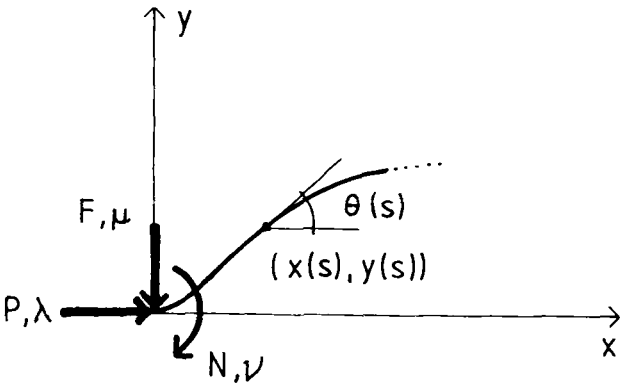

Fig. 2. A free body diagram for the buckled rod.

The unconstrained problem was originally posed and solved essentially completely by Euler, who, as Antman notes [Ant95], thus has a prior claim to Poincaré for invention of the qualitative theory of differential equations; he discovered many properties of elliptic functions before Jacobi.

In Section 3 we describe a numerical scheme developed for solution of rather general constrained problems, and give some examples to illustrate the analysis of Section 2. Then in Section 4 we discuss experimental results and compare them with the predictions of the model. Section 5 contains brief conclusions and identifies problems for future research.

The literature on nonlinear buckling and postbuckling is vast, but there is relatively little work on contact problems. A linear study of the pinned-pinned rod treated below appears in a "problems" book of Feodosyev [Feo77]; in Section 2.3 we show that our results reduce to his in the limit of small displacements. Keller and his colleagues have studied self-contact problems for rings [KFR72], the elastica [KF73], and more recently, thin sheets descending from a spool onto a rough surface [MK95]. The elastica work, in which the authors consider self-contact of the planar rod with clamped-clamped ends in its first mode, and with pinned-pinned ends in the third mode, is closest to that described below. In [KF73] a similarity solution for the shape of the rod between the contact points is found, load versus displacement bifurcation diagrams are computed numerically, and asymptotic expressions are developed for the contact point locations in terms of load.

2. Formulation of the Model

We recall the classical planar Euler buckling problem (cf. [Ant95], [Lov27]). Consider a deformed arc of an initially straight, uniform rod of flexural rigidity EI and length L subject to axial and lateral loads P, F, and moment N at the end $S = 0$, where S measures arclength. Taking moments at any point $S \geq 0$ and referring to the Cartesian coordinate system (x, y) and force sign convention of Figure 2, we have

$$EI\frac{d}{dS}\theta(S) + Py(S) + Fx(S) - N = 0, \tag{1}$$

where $\theta(S)$ denotes the slope at the point S and clockwise moments are positive. The position $(x(S), y(S))$ at S is obtained from the integral relations,

$$x(S) = \int_0^S \cos\theta(\sigma)\, d\sigma, \qquad \text{and} \qquad y(S) = \int_0^S \sin\theta(\sigma)\, d\sigma. \tag{2}$$

Differentiating (1), using (2), and defining nondimensional loads and moment via $\lambda = L^2P/EI$, $\mu = L^2F/EI$, and $\nu = LN/EI$, we obtain

$$\theta'' + \lambda \sin\theta + \mu \cos\theta = 0, \tag{3}$$

where $\theta'' = \frac{d^2\theta}{ds^2}$ and $s = S/L$ is the nondimensional arclength. This ordinary differential equation (ODE) can be posed as either an initial (IVP) or a boundary value problem (BVP). In the IVP, (3) is augmented by

$$\theta(0) = \theta_0, \qquad \theta'(0) = \nu, \tag{4}$$

and in view of standard ODE theory, it has a unique smooth solution $\theta(s) = \theta(s; \theta_0, \nu, \lambda, \mu)$, with $s \in [0, 1]$ corresponding to the physically relevant part of the solution. As noted by Kirchhoff (cf. [Lov27]), this is precisely analogous to the dynamical problem of the planar pendulum, with a shifted coordinate θ when $\mu \neq 0$. We appeal to this in developing a numerical scheme to construct solutions of the constrained problem in Section 3.

Equation (3) has the first integral

$$\frac{\theta'^2}{2} - \lambda \cos\theta + \mu \sin\theta = \text{const}, \tag{5}$$

on level sets of which its solutions necessarily lie. This permits the direct construction of phase portraits, but before giving examples, we introduce a sequence of BVPs from which we shall assemble the governing equations and solutions of the constrained problem. As noted in Section 1, we restrict ourselves to the case of symmetric, frictionless walls at $y = \pm h$, parallel to the line joining the endpoints.

There are five "elementary" BVPs from which full solutions will be built as sequences of solutions applying between end and/or contact points. The relevant boundary conditions (BCs) to supplement equation (3) are listed below. Three cases involve contact and admit special limits in which internal moments at contact points vanish.

As we have noted, the IVP solutions can be uniquely specified by the four scalars $\theta_0, \theta_0', \lambda, \mu$. In the case of a BVP we need the same number of scalar conditions, although they may not specify a solution uniquely. We list three of these conditions for each case between arbitrary endpoints $s = s_a$ and $s = s_b$:

(a) Pinned-pinned without contact:

$$\left.\begin{array}{rr} 1. & \theta'(s_a) = 0, \\ 2. & \theta'(s_b) = 0, \\ 3. & y(s_b) - y(s_a) = 0, \\ \text{or} & \mu = 0. \end{array}\right\} \tag{6}$$

(b) Clamped-pinned without contact:

$$\left.\begin{array}{rr} 1. & \theta(s_a) = 0, \\ 2. & \theta'(s_b) = 0, \\ 3. & y(s_b) - y(s_a) = 0. \end{array}\right\} \tag{7}$$

(c) Pinned-contact:

$$\left.\begin{array}{rr} 1. & \theta'(s_a) = 0, \\ 2. & \theta(s_b) = 0, \\ 3. & y(s_b) - y(s_a) = h. \end{array}\right\} \tag{8}$$

(d) Clamped-contact:

$$\left.\begin{array}{rr} 1. & \theta(s_a) = 0, \\ 2. & \theta(s_b) = 0, \\ 3. & y(s_b) - y(s_a) = h. \end{array}\right\} \tag{9}$$

(e) Contact-contact, same wall:

$$\left.\begin{array}{rr} 1. & \theta(s_a) = 0, \\ 2. & \theta(s_b) = 0, \\ 3. & \mu = 0. \end{array}\right\} \tag{10}$$

The fourth condition is identical in all cases and can be defined as

$$x(1) = d \qquad \text{or} \qquad \lambda = \lambda_0, \tag{11}$$

corresponding to the displacement (hard) boundary problem and the traction (soft or dead-load) problem, respectively.

We show typical element shapes and corresponding phase portraits in Figure 3, those for the degenerate zero internal moment cases being shown at far right. Note that the lateral load, μ, can take either sign in some cases, and the sense specified above is arbitrary. Correspondingly, for $\mu \neq 0$ the vertical axis of symmetry in the phase plane is shifted left or right from $\theta = 0$. A sixth case, contact-contact between opposite walls, is essentially identical to case (d), and (d), via symmetry about the inflection point, is in turn similar to case (c). In the explicit solutions developed below, solutions involving integer multiples of quarter circuits in the phase plane ((a) and (e)) are expressed in terms of complete elliptic integrals; the general cases ((b)–(d)) require incomplete elliptic integrals.

At a contact point the axial load and moment acting on an element must balance those on the adjacent element, but the lateral force μ may suffer a jump due to the net constraint force. This leads to a jump in shear force θ'', so that the resulting solutions $\theta(s)$ are only once-differentiable, the moment (curvature) $\theta'(s)$ being continuous.

In the physical experiments we are primarily interested in the displacement problem, in which the BVP for $s \in [0, 1]$ is controlled by the overall constraint

$$x(1) = \int_0^1 \cos\theta(s)\, ds = d \in (-1, 1], \tag{12}$$

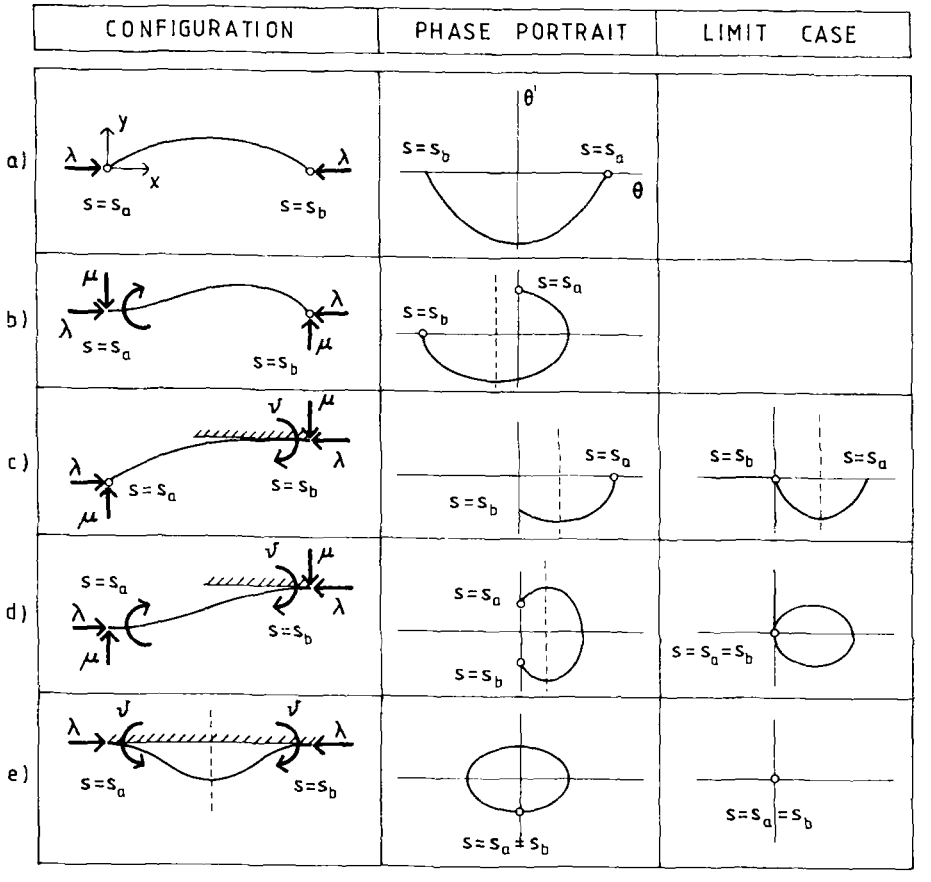

Fig. 3. Elemental BVPs and phase portaits for the constrained rod: (a) pinned-pinned (no contact); (b) clamped-pinned (no contact); (c) pinned-contact; (d) clamped-contact; (e) contact-contact (same wall). Limiting contact cases (c)–(e) shown in right column.

and the loads λ, μ are regarded as unknown, to be implicitly determined as part of the solution. However, it will be convenient to consider also the traction problem in which λ, μ are given and the displacements solved for directly. A third alternative is provided by path continuation, which our numerical approach adopts, as described in Section 3. This approach, in contrast with the previous two, does not admit jumps or snaps.

2.1. The Pinned-Pinned Case

Following the experimental protocol, we imagine monotonically decreasing the distance $d = x(1)$ between the endpoints, with fixed symmetric side-walls at a distance $\pm h$ from the centerline. Initially there is no contact, lateral forces and moments are zero, and the first half-wave is described by the elementary BVP (3)–(6), with $s_a = 0$; $s_b = 1/n$. Adopting $\mu = 0$, the lateral constraint $y(1) - y(0) = 0$ is satisfied automatically. Imposing reflectional symmetry about the midpoint of each half-wave implies that solutions for

all mode numbers n can be found at once. (For completeness, we mention that the alternative third boundary condition, $y(1) - y(0) = 0$, yields $\mu = 0$ except for the degenerate case at $x(1) = x(0)$, excluded from this paper; see, e.g., [Mad84] and [Dom94].) This classical problem has been solved many times since Euler's work, but in the appendix we recall some explicit details, since they do not seem readily available. We summarise key conclusions below.

There is a unique solution $\theta(s), \lambda$ to the displacement problem specified by (6) and (12) with $s_a = 0$, $s_b = 1$, for each $d \in (-1, 1)$ and mode n (denoting the number of half-waves). The exact solution is given in terms of elliptic integrals, and a simple approximation relating the end load and displacement may be found via their power series:

$$\lambda = n^2\pi^2\left[1 + \frac{(1-d)}{2} + \frac{9(1-d)^2}{32} + \mathcal{O}(|1-d|^3)\right]. \tag{13}$$

The exact analysis results in two critical loads and end displacements, the first being the classical Euler buckling load,

$$\lambda_n^b = n^2\pi^2, \qquad d_n^b = 1, \tag{14}$$

and the second the condition at which point contact with a side-wall first occurs,

$$\lambda_n^p = 4[nK(k)]^2, \qquad d_n^p = \left[\frac{2E(k)}{K(k)} - 1\right], \qquad \text{where } K(k) = \frac{k}{nh}. \tag{15}$$

Here $K(k)$ and $E(k)$ are the complete elliptic integrals of the first and second kinds respectively, and $k \in [0, 1]$ is the elliptic modulus. See [AS65], but note that the modulus defined there is $m = k^2$. In (15) $k = \sin(\theta(0)/2)$ and $\theta(0)$ is the slope at the endpoint. When $\lambda = \lambda_n^p$ we denote the corresponding value $\theta(0) = \theta_n^p$: This is used in the input data in Section 3.1.

We note that h can also be regarded as a control parameter, for example with $d < 1$ fixed. Equations (15) can then be used to determine critical values $h_n^p(d)$; in this case the elliptic moduli are found from the second equality and substituted into the third. In our experiments the value of h was always fixed. However, the critical values $h_n^p(d)$, interpreted as a function of d, have a global maximum, and this maximal value (which, for the sake of simplicity will be denoted by h_n^p) is of great interest both from the experimental and numerical point of view: If $h > h_n^p$ then contact is impossible for *any* d, while for $h < h_n^p$ (15) has two solutions k_n^p corresponding respectively to first contact and loss of contact in the nth mode with decreasing d (the latter may occur in the everted state $d < 0$).

The value h_n^p is found by simultaneous solution of the last equality of (15) and its derivative with respect to k,

$$\frac{d}{dk}K(k) = \frac{1}{k}\left[-K(k) + \frac{E(k)}{1-k^2}\right] = \frac{1}{nh}, \tag{16}$$

yielding the numerical values

$$k = 0.83745296\ldots \Rightarrow nh_n^p = 0.40314018\ldots. \tag{17}$$

It is interesting to note that this value of k, which characterises the unconstrained pinned-pinned beam at maximum lateral deflection, corresponds to an end angle of $\theta(0) = 113.74^{\circ}$ and a displacement of $d = 0.19469\ldots$, i.e., neither to $\theta(0) = \pi/2$, nor $d = 0$, which might seem plausible conjectures, but to a state between these two. (Also see [Lov27], Section 263.)

Once contact is made, a lateral force develops at the contact point, which must be balanced by lateral forces at the pins. The resulting elemental problem for the first quarter wave of the n-th mode is now completed by (8), with $s_a = 0$, $s_b = 1/2n$. The explicit solution involves incomplete elliptic integrals and is awkward to work with, except in a second limiting case when the internal moment at the contact point drops to zero. This occurs when the resultant of the axial and lateral forces passes through pin and contact point, leading to a third critical load and displacement given by,

$$\lambda_n^l = (1 - 2k^2)\,[4nK(k)]^2\,, \qquad d_n^l = \frac{nh(1 - 2k^2)}{k\sqrt{1 - k^2}}, \tag{18}$$

with corresponding end angle θ_n^l. Here the elliptic moduli satisfy

$$\frac{nh}{k\sqrt{1 - k^2}} = \left[\frac{2E(k)}{K(k)} - 1\right]. \tag{19}$$

As above, (19) can have two, one, or no solutions depending on h, the critical values $h_n^l < h_n^p$ being

$$k = 0.48967120\ldots \;\Rightarrow\; nh_n^l = 0.32107049\ldots, \tag{20}$$

derived by matching (19) and its derivative with respect to k.

If $h < h_n^l$, when d first drops below d_n^l, a (straight) segment of the rod makes contact with the wall (ultimately, for smaller d, line contact is lost again). The equilibrium conditions and the fact that the wall is flat and frictionless implies that the lateral force is now two equal point loads at the ends $s = s_1$ and $s = s_2 = \frac{1}{n} - s_1$ of a contact region throughout which the solution $\theta(s) \equiv 0$. Thus the end moments $\theta'(s_j) = 0$, and the resultant forces in each end element remain colinear with pins and contact points. In this régime the full solution is assembled from solutions to (8) with $s_a = 0, s_b = s_1$, followed by (10) with $s_a = s_1$, $s_b = s_2$, and again (8) with $s_a = 1$, $s_b = s_2$. In the phase space $[\theta, \theta']$ the full BVP consists of solutions to (3)–(8) running between $(\theta, \theta') = (2\theta_a, 0)$ and $(\theta, \theta') = (0, 0)$, and $(0, 0)$ and $(-2\theta_a, 0)$, along with flat segments $(\theta, \theta') \equiv (0, 0)$: the trivial solution of (3)–(10).

Here the slope at the end of the rod $\theta(0) = 2\theta_a$; indeed, as long as the internal moments at the ends of the contact line remain zero, we have

$$\tan(\theta(0)/2) = h/\Delta = \mu/\lambda, \tag{21}$$

where $\Delta = \int_0^{s_1} \cos\theta(s)\,ds$ is the axial distance subtended by the end segment. See Figure 3(c) and Equation (65) below. Again, the awkward exact expressions involving elliptic functions, as given in the appendix, can be approximated conveniently using the Taylor series, yielding the force-displacement relation,

$$\lambda = \frac{4\pi^2}{9n^2h^4}(1 - d)^2\left[1 - \frac{(1 - d)^2}{2n^2h^2} + \mathcal{O}(|1 - d|^4)\right]. \tag{22}$$

When each flat segment's length and axial load are such that it can buckle as a clamped-clamped beam in the first mode, as in Figure 3(e), a fourth critical load and displacement emerge, given by

$$\lambda_n^{sb} = \frac{4n^2\pi^2}{(1-2ns_1)^2}, \qquad d_n^{sb} = 1 + 2n(\Delta - s_1), \tag{23}$$

where

$$s_1 = \frac{hK(k)}{2k\sqrt{1-k^2}[2E(k) - K(k)]} \qquad \text{and} \qquad \Delta = \frac{h(1-2k^2)}{2k\sqrt{1-k^2}},$$

and the elliptic moduli are solutions of

$$nh\left[\frac{\pi}{2\sqrt{1-2k^2}K(k)} + 1\right] = k\sqrt{1-k^2}\left[\frac{2E(k)}{K(k)} - 1\right]. \tag{24}$$

Once more, (24) has two, one, or no solutions depending on whether $h < h_n^{sb}$, $= h_n^{sb}$, or $> h_n^{sb}$, where

$$k = 0.43505967\ldots \Rightarrow nh_n^{sb} = 0.14317822\ldots. \tag{25}$$

Following secondary buckling, the end element of each segment of length $\frac{1}{n}$ is governed by (8) and the central one by (10), the solutions of which must be matched via the internal moment $\theta'(s_1)$. A solution of this type persists until the central buckled portion first touches the opposite wall, a condition coinciding with first contact for the $3n$-th mode.

2.2. The Clamped-Pinned Case

This problem does not admit solutions as explicit as those obtained above, but the qualitative phase plane analysis is very similar. Again we start with the unconstrained problem (7), with $s_1 = 0$, $s_2 = 1$. The desired solution in the first mode is sketched in the phase plane of Figure 3(b); the second and higher modes simply make more circuits, but due to displacement of the center of symmetry, cannot be found as directly as in the pinned-pinned case. Nonetheless, as above we may identify several critical loads and displacements, the first being the classical clamped-pinned buckling load,

$$\tan\sqrt{\lambda_n^b} = \sqrt{\lambda_n^b} \Rightarrow \lambda_1^b \approx 2.045\pi^2, \ldots, \qquad d = 1, \tag{26}$$

obtained from the linearized ODE BVP derived from (3) and (7).

The second load λ_n^p, at which contact with a side-wall first occurs, is given by simultaneous solution of the following four equations for the unknown loads $\lambda = \lambda_n^p$ and $\mu = \mu_n^p$, the critical axial displacement $d = d_n^p$, and the parameter k (the elliptic modulus):

$$\sqrt{\tilde{\lambda}} = (2n+1)K(k) - F(\phi_a; k), \tag{27}$$

$$\lambda d = 2\sqrt{\tilde{\lambda}}[(2n+1)E(k) - E(\phi_a; k)] - \tilde{\lambda}, \tag{28}$$

$$\mu d = \sqrt{2(2k^2-1)\tilde{\lambda} + 2\lambda}, \tag{29}$$

$$\frac{\tilde{\lambda}^{\frac{3}{2}} h}{4n} = \mu[2E(k) - K(k)], \tag{30}$$

where $\tilde{\lambda} = \sqrt{\lambda^2 + \mu^2}$, $\tan\theta_a = \frac{\mu}{\lambda}$, $\sin\phi_a = \sin(\frac{\theta_a}{2})/k$, and $F(\phi; k)$ and $E(\phi; k)$ are the incomplete elliptic integrals of the first and second kinds, respectively [AS65]. As above, a critical value h_n^p exists, which determines if point contact can occur in specific cases. As for the pinned-pinned case, for $h < h_n^p$ no contact occurs, otherwise two critical loads (or displacements) are obtained, bounding an interval in which contact is maintained. Once contact is made at $s = s_1$ in the first mode, the BVP can be assembled from the elementary BCs (9) with $s_a = 0$, $s_b = s_1$, followed by (8) with $s_a = 1$, $s_b = s_1$.

As before, necessary conditions for onset of a flat segment on the wall, and secondary buckling of that segment, are obtained by requiring that internal moments vanish at the ends of the contact region. To avoid yet more unwieldly formulae, we restrict ourselves to the first buckling mode, in which only a single contact region occurs. Thus we have equivalent pinned-pinned rods of lengths $B_j = \sqrt{\Delta_j^2 + h^2}$, $j = 1, 2$, where $\Delta_1 = \int_0^{s_1} \cos\theta(s)\, ds$ and $\Delta_2 = \int_{s_2}^1 \cos\theta(s)\, ds$ are the axial distances subtended by the end segments, and we can appeal to the pinned-pinned theory. Note that the first element ($j = 1$) is in the *second* buckling mode while the second ($j = 2$) is in the *first* mode and the entire beam lies on one side of the central axis. As shown in the appendix, this leads to critical loads and overall axial displacements specified by simultaneous solution of

$$\lambda_1^l = (1-2k_1^2)\left[\frac{4K(k_1)}{s_1}\right]^2 = (1-2k_2^2)\left[\frac{2K(k_2)}{1-s_1}\right]^2, \tag{31}$$

$$d_1^l = \Delta_1 + \Delta_2, \tag{32}$$

$$s_1 = \frac{hK(k_1)}{2k_1\sqrt{1-k_1^2}\,[2E(k_1) - K(k_1)]}$$

$$= 1 - \frac{hK(k_2)}{2k_2\sqrt{1-k_2^2}\,[2E(k_2) - K(k_2)]}, \qquad \Delta_j = \frac{h(1-2k_j^2)}{2k_j\sqrt{1-k_j^2}}, \tag{33}$$

and

$$\lambda_1^{sb} = \frac{4\pi^2}{(s_2-s_1)^2} = (1-2k_1^2)\left[\frac{4K(k_1)}{s_1}\right]^2 = (1-2k_2^2)\left[\frac{2K(k_2)}{1-s_2}\right]^2, \tag{34}$$

$$d_1^{sb} = \Delta_1 + \Delta_2 + (s_2 - s_1), \tag{35}$$

$$s_1 = \frac{hK(k_1)}{2k_1\sqrt{1-k_1^2}\,[2E(k_1)-K(k_1)]}, \tag{36}$$

$$s_2 = 1 - \frac{hK(k_2)}{2k_2\sqrt{1-k_2^2}\,[2E(k_2)-K(k_2)]}, \qquad \Delta_j = \frac{h(1-2k_j^2)}{2k_j\sqrt{1-k_j^2}}. \tag{37}$$

The second pair of equations in (31) and equations (33) define three conditions which may be solved simultaneously for k_1, k_2, and s_1 (and hence Δ_1, Δ_2), given h. The critical load λ_1^l and displacement $d = d_n^l$ then follow from the first of (31) and (32). Similarly the last two equalities of (34) and equations (36)–(37) may be solved for $k_1, k_2, \Delta_1, \Delta_2$, s_1, and s_2, and the critical load and displacement found afterwards. As in Section 2.1, λ_1^l denotes the load at which the contact region may change from point to line, and λ_1^{sb} that at which secondary buckling can occur on the contact line segment. Recall that we only give results for the first mode $n = 1$ here. As in the pinned-pinned case, maximal critical values h_1^l and h_1^{sb} could be derived to characterize the possible contact behavior.

After developing these criteria for onset of line contact and secondary buckling, we performed the experiments described in Section 4. These revealed the presence of numerous additional (unsymmetrical) branches of solutions, and in the clamped-pinned case (Section 4.2), they showed that, while moments must indeed drop to zero at the contact point as d decreases (provided $h < h_1^l$), the line contact path is not followed; rather the moment changes sign at the clamped end and the beam crosses the center-line, thus developing a second inflection point and eventually a second contact point. See Sections 4 and 5 for further discussions.

The critical loads and displacements identified above and the analysis in the appendix provide checks for the numerically constructed solution branches in Section 3. In turn, the numerical data is compared with experiments in Section 4.

2.3. *Linearized Results*

Here we briefly show that the critical loads of Section 2.1 for the pinned-pinned problem coincide, in the appropriate limit, with those derived in a linearized analysis by Feodosyev ([Feo77], Problem 121). The limit is that of small lateral displacements: $y \le h \ll d \approx 1$ and small slopes $\theta \ll 1$, although θ depends more sensitively on the mode number than y. We observe that assuming $h \ll 1$ is equivalent to assuming that h lies below *all* critical values discussed earlier; thus, in the linear theory the number of contact points and segments can increase indefinitely.

Assuming end slopes $\theta_0 \ll 1$, we are concerned with the limit $h \to 0, k = \sin(\frac{\theta_0}{2}) \to 0$, with $\lim_{k\to 0} h/k$ finite, in which case $K(k) \to \frac{\pi}{2}$. Using this, we find that λ_n^p of (15) converges to the buckling load,

$$\lambda_n^p \to \lambda_n^b = \lambda_n^p(\text{linear}) = n^2\pi^2. \tag{38}$$

Applying the same limit in (18), we find

$$\lambda_n^l \to \lambda_n^l(\text{linear}) = 4n^2\pi^2, \tag{39}$$

and in (23)–(24),

$$\lambda_n^{sb} \to \lambda_n^{sb}(\text{linear}) = 16n^2\pi^2, \qquad s_1, \Delta \to \frac{1}{4n}. \tag{40}$$

In all cases linearization restricts $d = 1$, and so gives no meaningful predictions of end displacements.

These results agree with those obtained by direct solution of the standard linearized equation for the lateral displacement y in [Feo77], but an interesting point emerges. Feodosyev assumes that displacements follow the first buckling mode ($n = 1$) until, for $\lambda > \lambda_1^{sb}(\text{linear})$, the central flat region detaches and the rod switches to its third mode. This in turn changes to the ninth mode at $\lambda_3^{sb}(\text{linear})$, etc. Thus Feodosyev assumes that reflectional symmetry about the midpoint is preserved, and only modes $n = 1, 3, 9, \ldots$ are tabulated in his solution. In unloading, from say $\lambda \approx 4 \cdot 3^2\pi^2$, he assumes that the third mode persists to its linear buckling load $3^2\pi^2$, lower than the load $\lambda_1^{sb}(\text{linear}) = 16\pi^2$ at which it appeared, thus predicting hysteresis. Hysteresis is indeed observed in the experiments described below. However, other solutions having different symmetry, including those for $n = 2$, are also possible in this load range and are indeed observed in the experiments of Section 4. One cannot determine which branches are physically relevant without addressing the issue of stability.

2.4. *Stability*

In this paper we do not consider stability of equilibria in detail, but a few remarks are in order. The total stored energy is given by

$$E[\theta] = \int_0^1 \left[\frac{\theta'(s)^2}{2} + \lambda[\cos\theta(s) - 1] - \mu \sin\theta(s) \right] ds, \tag{41}$$

in which the first term is the strain energy due to curvature and the second two, energies associated with work done by the loading device. We have chosen the "constants" in these terms such that $E[\theta] = 0$ as long as no deflections occur, even if $\lambda \neq 0$. An equilibrium state $\bar{\theta}(s)$ is said to be *stable* if $E[\theta] \geq E[\bar{\theta}]$ for all nearby states θ, in a physically appropriate norm. Note that $\bar{\theta}$ need not be an absolute or global minimizer of E; local minimizers are also stable.

To illustrate a simple case, take the pinned-pinned beam without side-wall constraints ($\mu \equiv 0$) and subject to fixed (dead) end-load λ, suppose that $\bar{\theta}$ is an equilibrium, and consider $E[\bar{\theta} + \eta]$ for a small variation η satisfying the same boundary conditions. Substituting $\theta = \bar{\theta} + \eta$ into (41), expanding in η, and eliminating the $\mathcal{O}(\|\eta\|)$ term via integration by parts and use of the equilibrium equation (3), we arrive at

$$E[\theta] = E[\bar{\theta}] + \int_0^1 \left[\frac{\eta'(s)^2}{2} - \lambda \cos\bar{\theta}(s) \frac{\eta(s)^2}{2} \right] ds + \mathcal{O}(\|\eta\|^3). \tag{42}$$

Taking into account the boundary conditions (6), which imply the Poincaré inequality $\int_0^1 \eta'^2\, ds \geq \pi^2 \int_0^1 \eta^2\, ds$ for admissible variations, the quadratic form (second variation) is positive-definite if $\max|\lambda \cos\bar{\theta}(s)| < \pi^2$. It follows that the trivial solution up to

$\lambda = \pi^2$ is stable. The first mode equilibria, which bifurcate at $\lambda = \pi^2$, are also stable and remain so until $d = 0$. All higher mode branches are unstable. Analogous observations apply to the clamped-pinned and clamped-clamped beams without side-wall constraints. See Maddocks [Mad84], [Mad87] and Domokos and Gáspár [Dom94]. In fact Maddocks [Mad87] considers a related problem in which the $\theta(1)$ versus λ bifurcation diagram can "double back." He shows that the backward-going portions (λ decreasing as $\theta(1)$ increases) are unstable under dead loading, but stable under displacement (hard) boundary conditions of the type used in the experiments reported below.

In the presence of lateral forces due to side-wall contact or clamped boundaries, a calculation analogous to that above yields

$$E[\theta] = E[\bar{\theta}] + \int_0^1 \left[\frac{\eta'(s)^2}{2} - \left(\lambda \cos\bar{\theta}(s) - \mu \sin\bar{\theta}(s)\right) \frac{\eta(s)^2}{2} \right] ds + \mathcal{O}(\|\eta\|^3), \quad (43)$$

which must be constructed by piecing together the appropriate elementary equilibrium solutions, noting that the sign and value of μ may change as one moves from element to element. For displacement boundary conditions, the loads λ and μ must also be allowed to change when calculating the second variation. Unfortunately, the results of [Mad87] do not apply directly, since as one follows a given branch and contact is gained and/or lost, the governing equations change via jumps in the piecewise-constant lateral force $\mu(s)$. For example, it is well known that the second mode of the unconstrained pinned-pinned beam is unstable, while it is experimentally clear that the same mode is stable for the beam with two point contacts. The corresponding branch in the load-displacement graph is monotonically increasing in the neighborhood of (λ_2^p, d_2^p) where point contact is made, so it is not obvious that stability should change here. In fact, a secondary (asymmetrical) branch bifurcates at this point. See Section 5 (Figure 11) for further discussion.

3. Numerical Method

Elliptic functions are awkward to work with and must typically be evaluated numerically, so rather than using the analytical solutions of Section 2 directly, in practice we solve the BVP by integrating a sequence of IVPs $i = 1, \ldots, N$. We regard the unknown loads λ_i, μ_i, matching points s_i, and the undetermined initial condition $\theta(0) = \theta_0$ (for a pinned end) or $\theta'(0) = \nu$ (for a clamped end) as parameters to be varied in a shooting problem determined by the overall displacement and contact constraints. After outlining the numerical scheme, detailed in [DG95], we proceed as in Section 2, describing its application to the different phases of the loading process.

As already described, the problem can be reduced to a sequence of conventional BVPs on subsegments of the total arclength [0, 1], along with matching conditions. Each can be regarded as a parameter-dependent IVP starting at $s = s_a$ and ending at $s = s_b$, or as an input-output device. The input data are the initial conditions $\theta(s_a), \theta'(s_a)$, parameters λ, μ, and the integration constants $x(s_a), y(s_a)$. The output data are the same six scalars at $s = s_b$. (On each segment, λ and μ remain constant.) Using any convergent integrator for the IVP, the second set of six scalars can be determined with arbitrary precision as functions of the first six. Of course, certain initial conditions are fixed by the boundary conditions at $s = s_a$, so the output depends on fewer parameters in any particular BVP.

We will call the nonconstant initial values *variables* and remark that the location of a BVP's endpoint may also appear as a variable. The variables can be regarded as unknown quantities, needed to integrate the global IVP from $s = 0$ to $s = 1$. If we consider a sequence of IVPs, then the input for the subsequent IVP derives partly from the output of the previous one, and partly from new variables to be added. The matching conditions at intermediate points and the boundary conditions at $s = 1$ can be formulated as *functions* of the *output* scalars, thus, as functions of the variables. Hence, using the numerical integrator, our multipoint BVP can be reduced to a system of nonlinear algebraic equations.

In Sections 3.1 and 3.2 we specify variables and functions, respectively V and F in number, for the pinned-pinned and clamped-pinned elemental problems. As we will see, this procedure, although similar in many cases, requires some insight into the mechanical problem.

Fixing all four boundary conditions for each elementary BVP (3)–(6)—(3)–(10), we obtain isolated solutions. However, we are interested in continuous sequences of equilibria and we therefore omit the fourth condition (11), which is identical for each BVP. Recall that this condition prescribes either the load λ or the end displacement $x(1)$. With *one* condition relaxed, the equations yield a *one*-parameter family of solutions, called the *equilibrium path*. In practice, as control parameter we take neither λ nor $x(1)$ since, in general, the path may have turning points in both parameters.

The choice of algorithm depends largely on the question addressed. We posed the following (modest) question: "Given one equilibrium configuration (solution), provide an arbitrarily long sequence of equilibria, each of which is arbitrarily close to the adjacent ones." This task can be completed by a path-continuation method. In structural mechanics most path-continuation algorithms are based on extrapolation along the equilibrium path. Such algorithms are often referred to as incremental-iterative methods, since after each extrapolation step corrective iteration is necessary [Rik79].

The convergence properties of the iteration are often sensitive and need special attention. Here we applied the iteration-free "simplex" method of [DG95], which, in turn, is based on the so-called PL (piecewise-linear) algorithm (see [AG90]), as well as ideas from mechanics. The space spanned by the variables is subdivided into (small) simplices, the function values are computed at the vertices and the equilibrium path is linearly interpolated inside the simplices. Thus the method uses interpolation instead of extrapolation and provides the (approximate) equilibria via direct recursion. It delivers precisely one subsequent point. Since continuity (C^0) of the equilibrium paths is preserved in the piecewise-linear approximation, when approaching a bifurcation point on the primary path, the algorithm selects one of the (two) "exit" possibilities effectively at random and continues along the selected path. We note that the simplex method is also suitable for a more general task: finding *all* globally admissible equilibria in a given domain [Dom94].

To run the simplex method, for each member in the sequence of elementary BVPs we must specify:

- V *variables*, i.e., those initial conditions and parameters for all elementary BVPs which are not fixed by the boundary conditions at the initial points and not inherited from the previous segment, and in addition, those endpoint locations which are not fixed in advance,

- *F functions*, i.e., the matching conditions at intermediate points and the boundary conditions at $s = 1$, and
- the values of the variables at one equilibrium configuration.

In the following subsections we describe how this information can be obtained for our problem. Since we expect one-parameter families of solutions, the number V of variables has to exceed the number F of functions by one.

One further remark is relevant. When contact is established or lost as one follows a branch, the BVP, and hence the numbers V and F, change. The initial configuration of the new model is inherited from the final configuration of the previous one. We found that precision of 10^{-4} in initial parameters suffices to continue the computation. This is relatively easily maintained for force, moment, and angle; however, the contact point precision is limited by the mesh size of the discretization. Small mesh sizes increase computation time and lead to loss of accuracy via truncated Taylor series approximations of trignometric functions. In our computational environment (an IBM PC with Microsoft QuickBasic v 4.5 and DOS 6.2), mesh size and hence contact point accuracy could not be decreased below 10^{-3}. We therefore had to interpolate carefully in changing models. See [DG95] for general remarks on limitations of the simplex method.

3.1. The Pinned-Pinned Case

For simplicity we discuss only the first mode; higher modes can be treated in a similar manner. Starting with the contact-free configuration, the BCs are (6) with $s_a = 0$, $s_b = 1$. Adopting $\mu = 0$ as the third condition in (6) and fixing the initial point at $x(0) = y(0) = 0$, there remain two variables: $\theta_0 = \theta(0)$ and λ. The single boundary condition to be met at $s = 1$ is (6/2). Thus $V = 2$, $F = 1$, and consequently, $V - F = 1$. The initial configuration is specified by $(\theta_0, \lambda) = (0, 0)$. This case is illustrated in Figure 4(a). While following this equilibrium path the maximal transversal displacement has to be monitored. The symmetry with respect to $s = 0.5$ enforces $y_{\max} = y(0.5)$. At $y(0.5) = h$ the constraint is violated and this model becomes inapplicable.

Contact is established at this configuration with $\lambda = \lambda_1^p$. Symmetry reduces the computation to the first segment, described by (8) with $s_a = 0$, $s_b = 0.5$. Since a lateral force now acts, there are now three variables—θ_0, λ, and μ—and two boundary conditions to be met at $s = 0.5$—(8/2) and (8/3). Thus we have $V = 3$, $F = 2$, and consequently, $V - F = 1$. The initial configuration is specified by $(\theta_0, \lambda, \mu) = (\theta_1^p, \lambda_1^p, 0)$, the first two parameters being inherited from the last contact-free configuration. (Recall the definitions of λ_n^p and θ_n^p in and directly following Equation (15).) This situation is shown in Figure 4(b). The point-contact model is valid until $\theta'(0.5)$ changes sign, since this would imply an inflexion point at $s = 0.5$ and thus penetration of the boundary at $y = h$.

If $h < h_1^l$ then in the next phase line contact develops. Since symmetry with respect to $s = 0.5$ is still maintained, it is sufficient to compute the shape through the second contact point. Assuming that the first contact point is at $s = s_1$, the BCs are (8) with $s_a = 0$, $s_b = s_1$, followed by (10) with $s_a = s_1$, $s_b = 1 - s_1$. In (8) we now have four variables: Besides the previous three (θ_0, λ, μ), the location s_1 also appears as an input datum. In turn, we must satisfy three constraints: (8/2), (8/3), and (10/2). Thus we have $V = 4$, $F = 3$, and again $V - F = 1$. The initial configuration is specified

	CONFIGURATION	VARIABLES	FUNCTION(S)
(a)	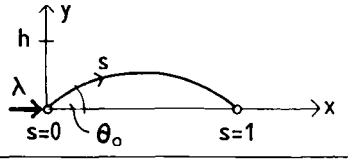	1. θ_o 2. λ	1. $\theta'(1)=0$
(b)	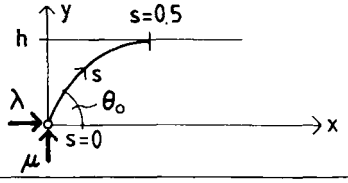	1. θ_o 2. λ 3. μ	1. $\theta(0.5)=0$ 2. $y(0.5)=h$
(c)	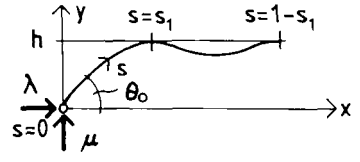	1. θ_o 2. λ 3. μ 4. s_1	1. $\theta(s_1)=0$ 2. $y(s_1)=h$ 3. $\theta(1-s_1)=0$
(d)	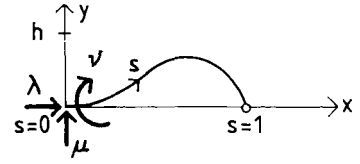	1. ν 2. λ 3. μ	1. $\theta'(1)=0$ 2. $y(1)=0$
(e)	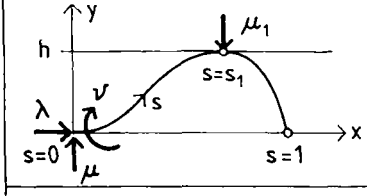	1. ν 2. λ 3. μ 4. s_1 5. μ_1	1. $\theta(s_1)=0$ 2. $y(s_1)=h$ 3. $\theta'(1)=0$ 4. $y(1)=0$
(f)	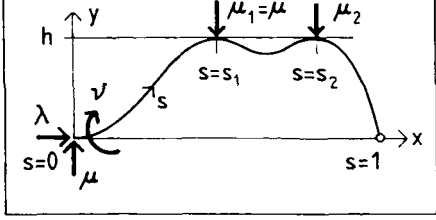	1. ν 2. λ 3. μ 4. s_1 5. s_2 6. μ_2	1. $\theta(s_1)=0$ 2. $y(s_1)=h$ 3. $\theta(s_2)=0$ 4. $\theta'(1)=0$ 5. $y(1)=0$

Fig. 4. Variables and functions used in the simplex method: (a) pinned-pinned (no contact); (b) pinned-pinned (point contact); (c) pinned-pinned (line contact); (d) clamped-pinned (no contact); (e) clamped-pinned (point contact); (f) clamped-pinned (line contact).

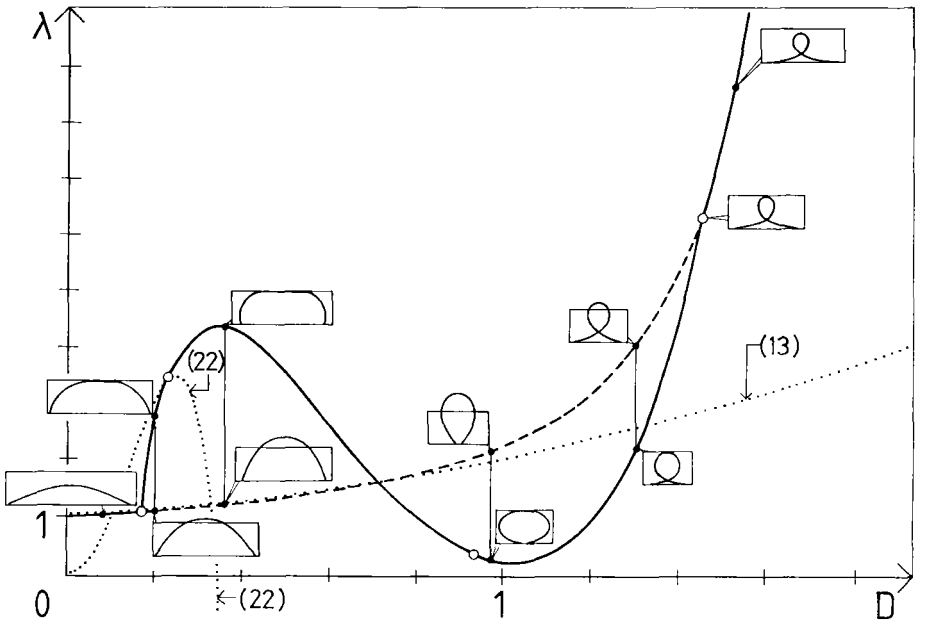

Fig. 5. Load-displacement curve for $h_1^{sb} < h = 0.25 < h_1^l$ in the pinned-pinned case. Constraint-free behavior plotted with dashed line. Onset (loss) of point and line contact indicated by open circles. Dotted curves indicate Taylor series approximations of (13) and (22); also see text.

by $(\theta_0, \lambda, \mu, s_1) = (\theta_1^l, \lambda_1^l, \mu_1^l, 0.5)$; the first four parameters are inherited from the last configuration of the point-contact-phase. Equation (18) also defines and allows direct computation of λ_1^l, θ_1^l.

From the computational viewpoint, secondary buckling of the flat, central portion requires no change in this model. We expect this phenomenon if $h < h_1^{sb}$. As mentioned before, at bifurcation points our algorithm follows one of the nontrivial branches (unless instructed otherwise). This configuration (illustrated in Figure 4(c)) remains valid until new contact is established at $s = 0.5$ with the opposite constraint wall. Then a new model has to be used, again with a different number of variables. This process can be continued; however, as the number of variables grows, the numerical scheme becomes slower and more sensitive.

In sharp contrast to the linearized model (cf. [Feo77], Subsection 2.3), in the nonlinear case the number of contact points (and the number of variables) does not grow indefinitely. Rather, after rising initially, in the limit $d \to -1$ all contact is lost and the model reverts to the classical Euler problem. To illustrate this, in Figure 5 we present a load-displacement curve computed for a case $h_1^{sb} < h < h_1^l$ $(h = 0.25)$. For comparison, we also show the analogous curve for a beam without lateral constraint. Physical configurations with equal end-displacements are displayed in the figure. The numerical data agree remarkably well with the critical values from the theory of Section 2.1. Equation (15) yields for λ_1^p the values 10.815 and 63.646 versus the numerical values of 10.814 and 63.229, respectively. From Equation (18) we obtain 34.531 and 3.956 for λ_1^l versus the numerical data 34.508

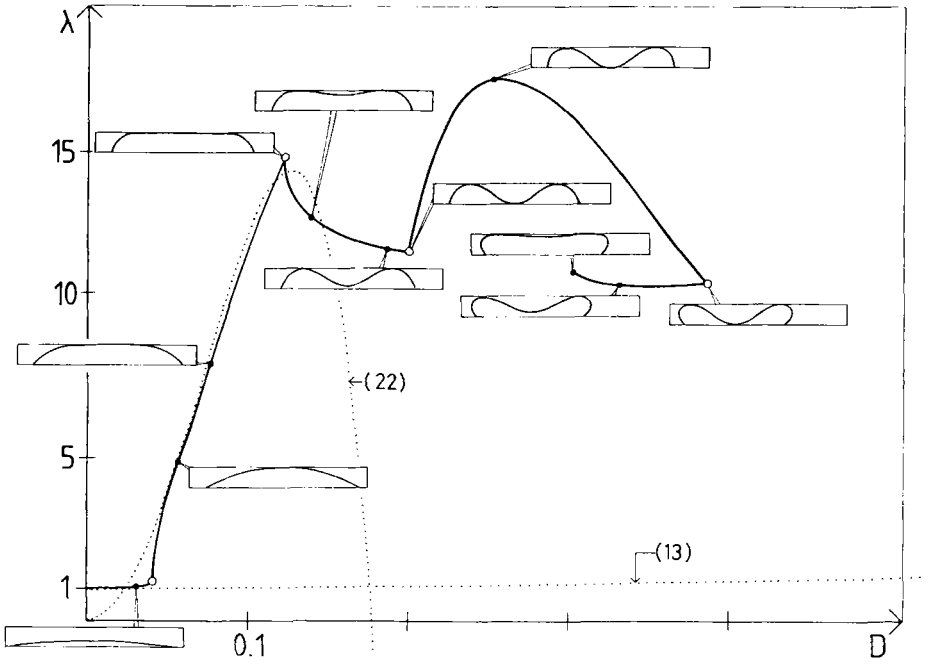

Fig. 6. Load-displacement curve for $h = 0.125 < h_1^{sb}$ and $h = 0$ in the pinned-pinned case (asymmetrical walls). Note horizontal and vertical tangencies. Onset of point contact and secondary buckling indicated by open circles. Dotted curves indicate Taylor series approximations of (13) and (22); also see text.

and 4.001. Agreement of the critical values for d is equally good. The unconstrained and line-contact segments predicted by the Taylor series expansions of (13) and (22) are shown on this and the following figure: They provide acceptable approximations for h smaller than about 0.125 (also see Figure 9).

Note that, here and henceforth, in place of the end displacement d we plot $D = 1 - d$ to agree with conventional load displacement curves of the engineering literature. We also specify all loads in units of $\lambda_1^b = \pi^2$, i.e., nondimensionalized on the pinned-pinned buckling load.

As a second example, in Figure 6 we show a load-displacement diagram and characteristic physical configurations for $h < h_1^{sb}$. In this numerical experiment the constraining walls are set asymmetrically: the upper one at $h = 0.125$, the lower one at $h = 0$. After following the previous scenario, the middle segment buckles and line contact is lost. It is worth noting that neither the load λ nor the end displacement d is monotonic along this equilibrium path, indicating that the sequence of equilibria can be realized experimentally only by switching from displacement to load control. The corresponding critical values are $\lambda_1^p = 10.069$, $\lambda_1^l = 38.499$, and $\lambda_1^{sb} = 146.641$, 110.051, compared with the numerically computed data 10.069, 38.475, and 145.72, 109.51. (We did not follow the branch far enough to observe the second values of λ_1^p and λ_1^l.)

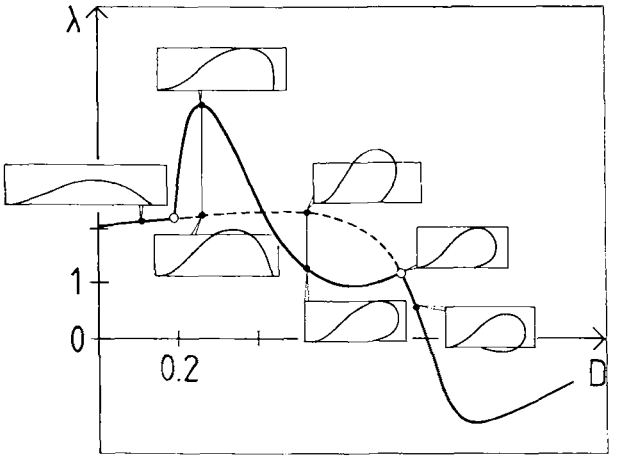

Fig. 7. Load-displacement curve for $h_1^l < h = 0.25 < h_1^p$ in the clamped-pinned case. Constraint-free behavior plotted with dashed line. Onset (loss) of point contact indicated by open circles.

3.2. The Clamped-Pinned Case

As in the previous subsection, we restrict our discussion to the first mode, although computations for higher modes have been done (see Section 4, Figure 10). In the initial, contact-free phase the BCs are (7) with $s_a = 0$, $s_b = 1$. After fixing the initial point at $x(0) = y(0) = 0$ there remain three variables: $\nu = \theta'(0)$, λ, and μ. The two boundary conditions to be met at $s = 1$ are (7/2) and (7/3); thus we have $V = 3$, $F = 2$, and, as before, $V - F = 1$. The initial configuration is specified by $(\nu, \lambda, \mu) = (0, 0, 0)$. This case is illustrated in Figure 4(d). This model remains valid until $y_{\max} = h$. Since there is no midpoint reflection symmetry, the location s_1 of the contact point is a priori unknown.

If $h < h_1^p$ contact is established at $\lambda = \lambda_1^p$, the location of the contact point being $s = s_1^p$. In this phase we need two elementary BVPs completed by (9) with $s_a = 0$, $s_b = s_1^p$ followed by a "reversed" (8) with $s_b = s_1^p$, $s_a = 1$; in this case $s_b < s_a$ and we integrate from s_b to s_a. There are five free variables: Besides ν, λ, μ, the location s_1, and the transversal contact force μ_1 are unknown when starting the IVP. Four constraints must be fulfilled: (9/2), (9/3), (8/1), and (8/3). The initial configuration is specified by $(\nu, \lambda, \mu, s_1, \mu_1) = (\theta_1^p, \lambda_1^p, \mu_1^p, s_1^p, 0)$. The first four parameters are inherited from the last configuration of the previous, contact-free phase, λ_1^p can also be determined by the solutions of Equations (27)–(30). This configuration is illustrated in Figure 4(e). As indicated in Section 2.2, the point-contact model remains valid until $\theta'(s_1)$ changes sign. Figure 7 illustrates a load-displacement curve with some characteristic physical shapes. Here $h = 0.25$; thus $h_1^l < h < h_1^p$. For comparison the unconstrained case with identical axial end displacement is also plotted. It is worth mentioning that the contact point moves back and forth as one proceeds along the branch: starting at $s_1^p = 0.593$, increasing to $s_1 = 0.642$, and returning to $s_1 = 0.483$.

If $h < h_1^l$ then the contact point splits into two, $s = s_1$, s_2, and the segment $s \in [s_1, s_2]$ lies flat against the constraint surface. Now we have three elementary BVPs: (3) with

(7) and $s_a = 0$, $s_b = s_1$, followed by (10) and $s_a = s_1$, $s_b = s_2$, and again a "reversed" (8) and $s_a = 1$ and $s_b = s_2$. Since in (10) $\mu = 0$, the contact force μ_1 at s_1 is identical to μ. When integrating the IVP from $s = 0$ the following six variables are unknown: $\upsilon, \lambda, \mu, s_1, s_2, \mu_2$, the last one denoting the contact force at $s = s_2$. Using these variables five conditions must be met: (9/2), (9/3), (10/2), (8/1), and (8/3). The configuration is shown in Figure 4(f). As in the pinned-pinned case, this path could be followed further, with an increasing number of variables as the number of contact points increases; moreover, as noted in Section 2.2, another branch, with a second critical point, bifurcates from this branch at the point where the moment at the clamped end drops to zero; see Section 4.2 and Figure 10.

4. Experimental Results

Buckling measurements were made using long, slender rectangular stainless steel beams with dimensions of circa 0.05 × 6.25 × 100 mm, shape-constrained to deform in a plane. Buckling was further constrained by rigid walls on either one or both sides placed parallel to and at controlled distances from the beam's center-line. The forces required to maintain a given deformed state were measured using a modified Ohaus CT 200 strain-gauge balance assembly in contact with one end of the beam, contact being with a shallow vertical vee groove approximating a pinned boundary condition. The other end was either supported by a rotary jewelled bearing, or clamped parallel to the deformation axis, depending on the desired boundary conditions.

Both balance assembly and support could be moved with either displacement or displacement rate under control. Balance motion was effected by a Newport motor-micrometer used in either the jog or continuous modes. In the former, step sizes were varied between 2 and 500 microns. Since the strain-gauge balance deflected with increasing load, it was necessary to correct to obtain the true beam end displacement. This was achieved by measuring the force recorded by the balance as it was advanced into a rigid constraint and correcting all displacements for balance deflections at their measured load values. After correction, the loading device approximates hard (displacement) boundary conditions. The experiment was mounted on an optical breadboard table to provide a stable base. The apparatus is shown in Figure 8.

To minimize the effects of friction between beam and side-walls, the latter were made from glass microscope slides treated with a molybdenum disulfide solid lubricant. In jog mode the system was vibrated after each position step using an electric bell motor to minimise hysteresis due to mechanical backlash in the motion stage and friction bewtween beam and constraint. The resulting force/position data pairs were recorded, along with video images and other information regarding the beam's shape.

Typically, the beam is inserted with its long axis parallel to the motion axis and the larger cross-sectional axis vertical, so that buckling occurs in a horizontal plane, thus minimizing gravitational effects. The stationary end is placed in the pivot, or clamp, and the balance end advanced using the motor micrometer until the beam just contacts the vee groove in the thrust pad. In this condition there is a pre-load of about 0.5g. The vertical glass side-walls are placed at equal distances from the center-line and parallel to it. The balance end displacement is then incrementally increased (decreasing the axial

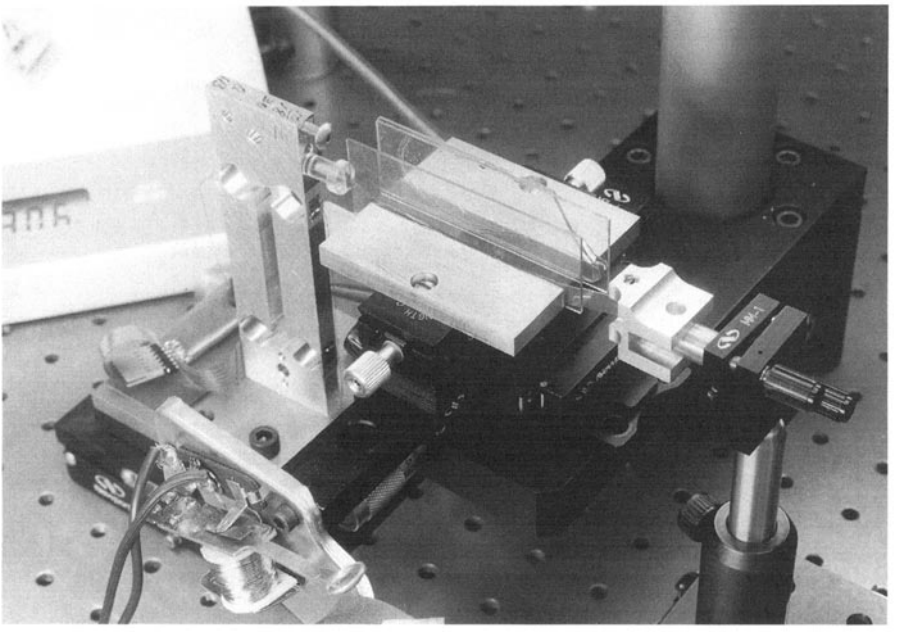

Fig. 8. The experimental apparatus.

length d) in jog mode with data taken following shakedown after each step. Such hard loading allows one to investigate regions in which the corresponding equilibria under soft (traction) loading are unstable.

After maximum displacement (minimum d) is achieved, the process is reversed to detect hysteresis and mode jumping to other equilibrium branches. Throughout, the system remains in the elastic range, but several contact events may occur. Prior to such runs, preliminary surveys of beam response were recorded on videotape under constant strain-rate conditions, and regions for detailed study in the stepping mode were selected from this data.

The flexural rigidity (EI) of the samples is a critical experimental parameter. It was estimated by clamping the beam at one end and measuring the frequency of small amplitude cantilever vibrations as a function of free length. Beam deflection was measured by shining a HeNe laser on the surface and imaging the laser spot on a photo-diode through an interference filter so that it was bisected by a knife edge. The resulting (slowly decaying) periodic signal was recorded on a digital oscilloscope that also determined the frequency. A least squares fit of the data, plotted as frequency squared against the inverse fourth power of free length according to simple linear theory (e.g., [Tho65], Section 8.5) provided the product EI. This method proved more accurate than direct measurement of the cross-sectional dimensions and use of tabulated Young's moduli.

In the following subsections we compare experimental results, in the form of load-displacement curves, with the theoretical and numerical calculations. The two specific cases illustrated in Figures 9 and 10 are typical of several runs.

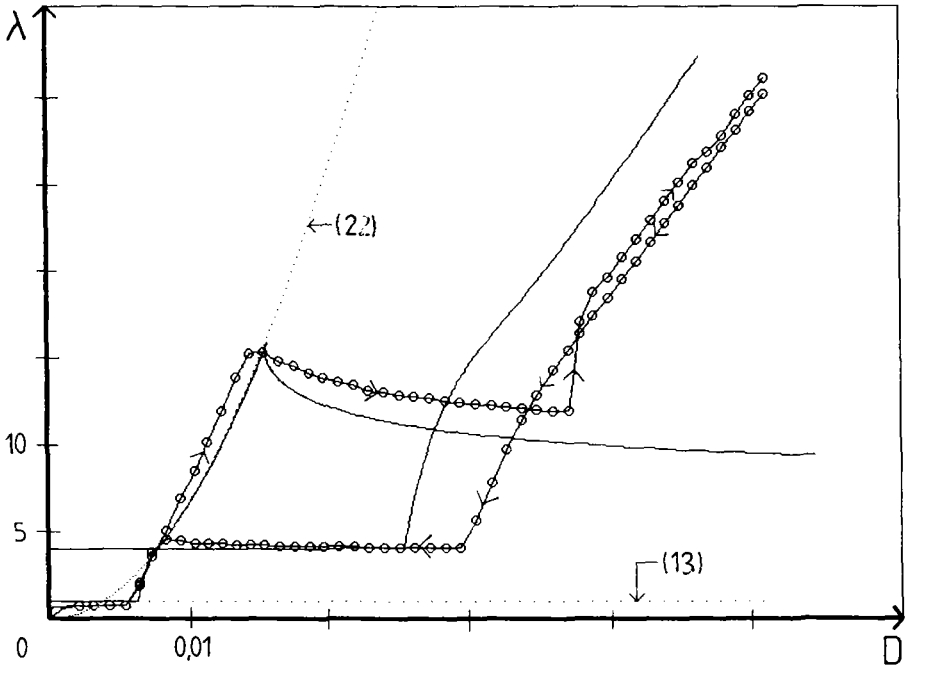

Fig. 9. Load-displacement curves for a pinned-pinned beam: $h = \pm 0.05$; solid curves with circles correspond to experiments. Arrows indicate direction of loading history. Numerical results are shown as solid curves. Taylor expansions of equations (13) and (22) are shown as dotted lines.

4.1. The Pinned-Pinned Case

Figure 9 shows results for a pinned-pinned beam with symmetric side-walls at nondimensionalized distances $h = \pm 0.05$. The load is normalized by the first Euler buckling load $\pi^2 EI/L^2$, with EI estimated as noted above, and the displacement has been corrected for balance flexibility and similarly normalized by the length L. As in the previous figures, we plot the end displacement ($D = 1 - d$). The comparison among analytical, numerical, and experimental critical values is summarized in Table 4.1. The beam has some unavoidable initial curvature (imperfection), with the result that (D) increases continually rather than exhibiting a sudden bifurcation. Nonetheless, it closely follows the theoretical prediction, with the load remaining essentially constant after initial buckling until the beam's center contacts one side-wall. At this point there is an abrupt change in the slope of the load/displacement curve, which then increases monotonically with the beam contacting and subsequently flattening against the wall. (The change from point to line contact is hard to detect visually, but appears to coincide with a slight upturn in slope in some experimental runs.)

This continues until the central section undergoes secondary buckling, after which the load decreases as the amplitude of the center buckle grows. At $D \approx 0.038$, before the central section contacts the opposite side-wall, a jump to the second mode occurs. The two contact portions then flatten and increase in length as D continues to increase until

Table 4.1. Critical values for the pinned-pinned case, $h = 0.05$.

	Analytical	Numerical	Experimental
Point Contact			
λ_1^p	1.003	1.003	0.7836
D_1^p	0.0062	0.00619	0.0053
λ_2^p	4.052	4.050	4.080
D_2^p	0.0251	0.0251	0.0258
Line Contact			
λ_1^l	3.985	3.983	3.620
D_1^l	0.075	0.0755	0.072
λ_2^l	15.75	15.76	14.23
D_2^l	0.0355	0.0309	0.0354
Secondary Buckling			
λ_1^{sb}	15.875	15.837	15.254
D_1^{sb}	0.0155	0.0154	0.0151

the limit of travel of the motor is reached. Reversing displacements, the beam follows the second mode path down past the line/point contact transition until contact is lost at one wall, after which it remains close to the almost horizontal unconstrained second mode branch, with $\lambda \approx 4\pi^2$. Along this branch the experimental shape is a mixture of first and second modes, initially predominantly second, but with the relative contribution of the first mode growing so that the contact point moves toward the center until the path rejoins the first mode branch, which it then follows back to (0, 0).

Comparison with theory is good on the first mode branch, including the portion on which the load drops after secondary buckling occurs. The second branch, including points (d_2^p, λ_2^p) and (d_2^l, λ_2^l), is however significantly displaced to the left of the experimental curve, so that, while the λ values compare well, the d values are in error. We believe that this is primarily due to asymmetry of the specimen. Recalling the sensitive dependence on h revealed in the denominator of Equation (22), it seems reasonable that initial curvature should have a large effect via its influence on the effective value of h; indeed, a series of experiments with identically spaced constraint walls laterally shifted with respect to the beam centerline revealed variations of up to 15% in the position of this portion of the second mode branch.

4.2. The Clamped-Pinned Case

Figure 10 shows typical load-displacement data from a clamped-pinned experiment. Here $h = 0.053 < h_2^l$, and we observe both single and double point contact and line contact configurations. As noted in Section 2.2, after point contact is established in the first mode at $D \approx 0.0075$, the solution follows a smooth branch in which the moment $\theta'(0)$ at the clamped end drops to zero and then changes sign, so that a second critical point, nearer the clamped end, appears at $D \approx 0.011$, in the almost flat portion of the experimental curve. This second critical point first contacts the wall on its side at

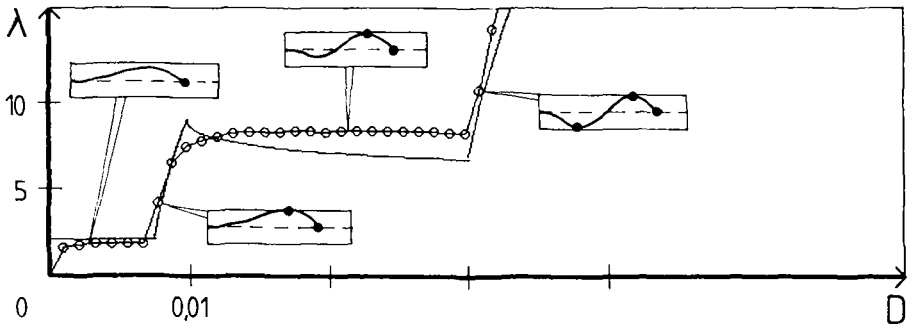

Fig. 10. Load-displacement curves for a clamped-pinned beam: $h = \pm 0.053$. Solid curves with circles correspond to experiments. Numerical results are shown as solid curves. Filled circles on inset diagrams indicate contact points and pin support.

$D \approx 0.030$, after which the beam's shape is essentially that of the second clamped-pinned mode. Thereafter the curve rises steeply, with line contact being established at both contact locations above about $D = 0.035$. Unloading, the beam follows the same path without hysteresis.

Also shown on Figure 10 are numerically computed load-displacement curves. The portions of the curve below $D \approx 0.01$ come from the first mode computation described in Section 3.2, and correspond to the theory of Section 2.2. Plotting of this branch terminates at $D, \lambda \approx 0.011, 8.86$, where the moments at the clamped end and the contact point drop to zero. As described in Section 2.2, the branch continues with a region of line contact, but, taking our cue from the experiment, here we switch to an "asymmetrical" second mode branch with two critical points, which follows a gently descending path to establishment at $D, \lambda \approx 0.029, 6.83$ of the second contact point nearer the clamped end, after which the second mode branch is followed. Key critical values from experiment and numerical computation from the model are summarised in Table 2 (closed form theoretical results are not available for this case).

To understand how the asymmetric first/second mode branch in Figure 10 differs from the "pure" second mode branch, it is necessary to note that the latter contains, at $D, \lambda \approx$

Table 4.2. Critical values for the clamped-pinned case, $h = 0.053$.

	Numerical	Experimental
Point Contact		
λ_1^p	2.051	1.866
D_1^p	0.0073	0.0065
λ_2^p	6.828	8.198
D_2^p	0.0293	0.0294
Line Contact		
λ_1^l	8.86	7.93
D_1^l	0.011	0.0095

6.089, 0.01602, a point where contact first occurs at the critical point nearest the clamped end, whereas along the branch shown contact is always at the critical point nearest the pinned end. The pure second mode branch is intersected at D, $\lambda \approx 6.089, 0.01602$ by a further asymmetric branch containing "unphysical" states with point contact maintained by forces directed *towards* the walls. The complete bifurcation diagram therefore contains at least three double-critical-point branches, only one of which—the one we believe relevant to experiment—is shown in Figure 10.

5. Conclusions

The results reported above demonstrate an acceptable match between experiment and theory. The major "uncontollable" factors in the experiments, omitted from our model, are friction with the side-walls and imperfections (asymmetries) of the specimens. A simple static friction model would give lateral forces, proportional to the normal contact forces μ, which could clearly affect equilibrium states and critical loads and displacements, especially those corresponding to secondary buckling of the flat segment in pinned-pinned experiments. We therefore believe that the primary responsibility for experimental loads generally exceeding theoretical ones lies with friction. We have already commented in Section 4.1 (Figure 9) on the influence of asymmetries in shifting load-displacement curves laterally.

In comparing experiment and theory above, we have included only stable and "physical" configurations, since unstable equilibria cannot be realised experimentally. However, unstable and even unphysical equilibria, such as those requiring *negative* constraint forces (forces directed *towards* the walls) and those involving penetration of walls near points of tangency, are relevant in developing the full global understanding of the interrelations and bifurcations of branches in the load-displacement diagram for any given case. The model predicts *all* equilibria and it is therefore of interest to compute as many as possible and determine their stability properties in order to interpret observations such as mode-jumping and hysteresis.

To this end, Figure 11 shows a large number of secondary branches captured numerically for the pinned-pinned beam. These branches originate from two points labelled 11 and 14: where the primary second and third mode branches make simultaneous multiple contacts with the constraint walls. Segments of some of these branches (1, 2, 3, 4, 10, 11, 12) were shown earlier in Figure 9; another one (13) was observed in another experiment. These branches, corresponding to asymmetric equilibria, are absent in the linearized model discussed in Section 2.3. As $h \to 0$, the number of asymmetric branches grows (they become admissible for higher and higher buckling modes); however, the difference between them decreases. Finally, as we reach the limit corresponding to the linear model, all those belonging to the same mode collapse to a single symmetric solution. Similar observations apply to the clamped-pinned case. It is interesting to ask, which of these asymmetrical branches are stable and hence physically relevant?

The difficulty of stability analysis arises from the fact that, while the problem is continuous, the relevant functions are nonsmooth due to contact forces. Thus the standard tools for stability analysis of continua are useless. Nor can techniques for discrete structures be applied directly either. We envisage a mixed approach to this problem, which we

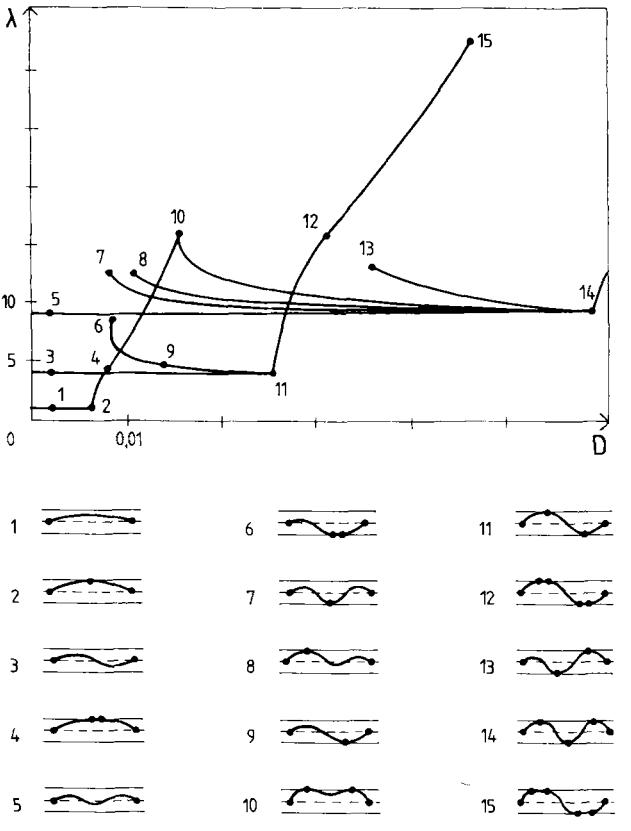

Fig. 11. Numerical load-displacement curves for the pinned-pinned beam: $h = \pm 0.05$; Numbered points on branches correspond to physical shapes indicated.

hope to treat in a forthcoming paper. Here we outline briefly an algorithm which yields some insight even without performing any computations.

As in the model developed in Section 2, we regard the beam as a structure composed of elements, starting and ending at contact points and the endpoints of the beam. At contact points a *node* connects two adjacent elements. A *necessary* condition for the stability of the structure is the stability of each element individually, with nodes fixed. If any element is in an unstable configuration, the structure as a whole is also unstable. The stability of each element can be investigated by standard tools of continuum mechanics, and even without detailed computation, in some cases it can be derived by observation.

If the necessary condition for stability is satisfied, one can seek a sufficient condition for global stability. In this step we regard the beam as an assembly of nodes connected by nonlinear springs, transmitting forces as well as moments, whose stiffnesses are determined via the elemental BVPs. This structure has $2n$ degrees of freedom, n denoting the number of contact points, where each point can *slide* and/or *roll* along the constraining walls. Stability of this discrete structure is determined by the eigenvalues of its $2n \times 2n$

Hessian matrix, which can be found numerically. Positive-definiteness of the Hessian supplies the *sufficient* condition for stability. It is important to note that analysis of the Hessian is meaningful only if the individual segments are stable.

Based on the necessary condition (stability of individual segments), in Figure 11 we can tell that branches 3, 5, and 8 are unstable (for 3 and 5 this is a trivial observation, in the case of 8, a nontrivial one). The stability of the remaining equilibria requires calculation of the Hessian, a substantial task. We hope to address this, and the stability question in general, in a future paper. We also intend to investigate the interrelations of asymmetrical and unphysical branches of equilibria such as those shown in Figure 11 for both pinned-pinned and clamped-pinned cases, and to perturb the symmetric, parallel side-walls considered thus far, in an attempt to derive more complete unfolding and bifurcation diagrams.

In closing, we remark that it is difficult to make a clean distinction between "analytical" and "numerical" techniques in this problem. The theory of Section 2 results in nonlinear algebraic equations containing elliptic integrals. The numerical technique of Section 3 also leads to systems of nonlinear algebraic equations containing special functions. In the latter case the function values are obtained by integrating an IVP for a finite segment; the solutions of the relevant ODEs being, naturally, elliptic functions. Thus, while the two approaches presented here emphasize different aspects, it seems difficult to place them in entirely different categories.

Appendix: Computational Details

The Pinned-Pinned Case

We sketch some details of explicit solutions to the BVPs (3), (6)–(10). We deal first with the pinned-pinned case of (6), for which the first integral (5) reduces to

$$\frac{\theta'^2}{2} - \lambda \cos\theta = -\lambda \cos\theta_0, \tag{44}$$

where $\theta_0 = \theta(0) = -\theta(1)$, by symmetry of reflection about the midpoint $s = \frac{1}{2}$. From (44) derives the quadrature,

$$\int_{\theta_0}^{\theta(s)} \frac{d\theta}{2\sqrt{\lambda[\sin^2(\frac{\theta_0}{2}) - \sin^2(\frac{\theta}{2})]}} = \int_0^s d\sigma, \tag{45}$$

which, via the transformation $\sin(\frac{\theta}{2}) = \sin(\frac{\theta_0}{2})\sin(\phi)$, may be evaluated as

$$\int_{\phi(s)}^{\frac{\pi}{2}} \frac{d\phi}{\sqrt{1 - k^2 \sin^2\phi}} = F(\pi/2; k) - F(\phi(s); k) = \sqrt{\lambda} s, \tag{46}$$

where F denotes the incomplete elliptic integral of the first kind and $k = \sin(\frac{\theta_0}{2}) \in [0, 1]$ is the elliptic modulus [AS65]. To satisfy the BVP (3) and (6) we require $\theta'(1) = 0$, implying, via symmetry, that $\theta(s)$ has internal zeros at $s = \frac{1+2j}{2n}$; $j = 0, \ldots, n-1$

for the n-th buckling mode. When $\theta = 0$ (resp. θ_0), $\phi = 0$ (resp. $\frac{\pi}{2}$), and, from (46), it therefore follows that

$$K(k_n) = \frac{\sqrt{\lambda}}{2n}, \tag{47}$$

where $K(k) = F(\frac{\pi}{2}; k)$ is the complete elliptic integral of the first kind and $\theta_{0n} = 2\sin^{-1}(k_n)$ is the slope at the end of the beam subject to axial load λ, in the n-th mode. From the limit $K(0) = \frac{\pi}{2}$ we derive (14).

Appealing to symmetry and using the relation

$$\frac{d\theta}{ds} = 2\sqrt{\lambda\left[\sin^2\left(\frac{\theta_0}{2}\right) - \sin^2\left(\frac{\theta}{2}\right)\right]}$$

from (44), the displacement constraint (12) may be written as

$$d = \frac{2n}{\sqrt{\lambda}} \int_0^{\theta_0} \frac{\cos\theta \, d\theta}{2\sqrt{\sin^2(\frac{\theta_0}{2}) - \sin^2(\frac{\theta}{2})}}. \tag{48}$$

After trignometrical manipulation and use of the same transformation as above, this integral evaluates as

$$\int_0^{\frac{\pi}{2}} \left[2\sqrt{1 - k^2\sin^2\phi} - \frac{1}{\sqrt{1 - k^2\sin^2\phi}}\right] d\phi = [2E(k) - K(k)], \tag{49}$$

where $E(k)$ is the complete elliptic integral of the second kind. From (47), we then obtain the equation

$$d = \left[\frac{2E(k)}{K(k)} - 1\right], \tag{50}$$

from which $d = d_n$ may be found directly for each $k = k_n$ satisfying equation (47). Alternatively, since $E(k)$ monotonically decreases and $K(k)$ monotonically increases with k, (50) may be solved uniquely for $k = k_d$ in terms of $d \in (-1, 1)$, and an infinite sequence of loads

$$\lambda_n(d) = 4n^2(K(k_d))^2 \tag{51}$$

consistent with this displacement in each given mode, may be found from (47). These provide direct solutions to the displacement BVP. Note that, as $\theta_0 \to 0$ ($k \to 0$), E and K both approach $\frac{\pi}{2}$, giving $d = 1$, as expected for the undeformed rod. As $\theta_0 \to \pi$ ($k \to 1$), $E \to 1$ and $K \to \infty$, so that $d \to -1$, again as expected for the "everted" state (cf. [Lov27]). It is interesting to note that, from (50), the end angle $\theta_0 = 2\sin^{-1}(k_d)$ for a given displacement d is identical in *every* mode.

For relatively small k (θ_0), the truncated power series for the elliptic integrals

$$K(k) = \frac{\pi}{2}\left[1 + \frac{k^2}{4} + \frac{9k^4}{64} + \mathcal{O}(k^6)\right] \quad \text{and} \quad E(k) = \frac{\pi}{2}\left[1 - \frac{k^2}{4} - \frac{3k^4}{64} + \mathcal{O}(k^6)\right] \tag{52}$$

provide the simple approximation

$$d = 1 - k^2 - \frac{k^4}{8} + \mathcal{O}(k^6)$$

to (50). Using this in (47), we obtain

$$\lambda = n^2\pi^2\left[1 + \frac{(1-d)}{2} + \frac{9(1-d)^2}{32} + \mathcal{O}(|1-d|^3)\right]. \tag{53}$$

The condition for first contact in the n-th mode is derived from (3) and (8) with $\mu = 0$, $s_a = 0$, and $s_b = \frac{1}{2n}$. Substituting for $\sin\theta$ from the ODE and integrating gives

$$\left|y\left(\frac{1}{2n}\right)\right| = \left|\int_0^{\frac{1}{2n}} \sin\theta(s)\,ds\right| = \left|\int_0^{\frac{1}{2n}} \frac{\theta''(s)}{\lambda}\,ds\right| = \left|\frac{\theta'(\frac{1}{2n})}{\lambda}\right| = h, \tag{54}$$

or, via (44),

$$\sin\left(\frac{\theta_{0n}}{2}\right) = k_n = \frac{\sqrt{\lambda}h}{2}. \tag{55}$$

Satisfying (55) and (47) simultaneously and using (50) yields (15).

The pinned-contact problem with $\mu \neq 0$ can be reformulated by letting $\psi = \theta - \theta_a$, $\tan\theta_a = \frac{\mu}{\lambda}$, so that (8) becomes

$$\begin{aligned} \psi'' + \tilde{\lambda}\sin\psi = 0: \qquad & \tilde{\lambda} = \sqrt{\lambda^2 + \mu^2}, \\ \psi'(0) = 0, \qquad & \psi(\tfrac{1}{2n}) = -\theta_a, \end{aligned} \tag{56}$$

with displacement constraints

$$x(1) = \int_0^{\frac{1}{2n}} \cos(\psi + \theta_a)\,ds = \frac{\lambda}{\tilde{\lambda}}\int_0^{\frac{1}{2n}} \cos\psi\,ds - \frac{\mu}{\tilde{\lambda}}\int_0^{\frac{1}{2n}} \sin\psi\,ds = \frac{d}{2n}, \tag{57}$$

$$y(1) = \int_0^{\frac{1}{2n}} \sin(\psi + \theta_a)\,ds = \frac{\lambda}{\tilde{\lambda}}\int_0^{\frac{1}{2n}} \sin\psi\,ds + \frac{\mu}{\tilde{\lambda}}\int_0^{\frac{1}{2n}} \cos\psi\,ds = h, \tag{58}$$

and we may appeal to the theory for the pinned-pinned case. Following the computations of (45)–(46) and (48)–(49), and recognising that the desired solutions make between one and two quarter turns, we obtain

$$K(k) + F(\phi_a; k) = \frac{\sqrt{\tilde{\lambda}}}{2n} \tag{59}$$

and

$$\int_0^{\frac{1}{2n}} \cos\psi\,ds = \frac{1}{\sqrt{\tilde{\lambda}}}[2E(k) - K(k) + 2E(\phi_a; k) - F(\phi_a; k)], \tag{60}$$

$$\begin{aligned} \int_0^{\frac{1}{2n}} \sin\psi\,ds &= -\frac{\psi'(s)}{\tilde{\lambda}}\Big|_0^{\frac{1}{2n}} = \frac{2k}{\sqrt{\tilde{\lambda}}}\left[\cos\phi\,\Big|_{\frac{\pi}{2}}^{\phi_a}\right] = \frac{2k}{\sqrt{\tilde{\lambda}}}\cos\phi_a \\ &= \frac{2}{\tilde{\lambda}}\sqrt{\frac{(2k^2-1)\tilde{\lambda} + \lambda}{2}}, \end{aligned} \tag{61}$$

where $F(\phi_a; k)$ and $E(\phi_a; k)$ are incomplete elliptic integrals of the first and second kinds, $k = \sin(\frac{\psi_0}{2})$, and $\sin\phi_a = \sin(\frac{\theta_a}{2})/\sin(\frac{\psi_0}{2})$. Hence, from (57)–(58) we have

$$\lambda d + 2n\mu h = 4n\sqrt{\tilde{\lambda}}[E(k) + E(\phi_a; k)] - \tilde{\lambda} \text{ and} \tag{62}$$

$$2n\lambda h - \mu d = 4n\sqrt{\frac{(2k^2 - 1)\tilde{\lambda} + \lambda}{2}}. \tag{63}$$

Simultaneous solution of (59) and (62)–(63) yields k, λ, and μ in terms of h, d and n. Note that, when $\mu = 0$, these expressions reduce to (15).

When the resultant of the axial and lateral forces passes through pin and contact point, we have

$$d\mu = 2nh\lambda \qquad \text{and} \qquad \tan\theta_a = \tan\psi_0 = \frac{2nh}{d}, \tag{64}$$

so that $\phi_a = \frac{\pi}{2}$, $\tilde{\lambda} = \lambda\sqrt{d^2 + 4n^2h^2}/d$, and (59) and (62)–(63) reduce to (18)–(19).

When line contact occurs, we use the geometric condition analogous to (64),

$$\tan\theta_a = \frac{h}{\Delta} = \frac{\mu}{\lambda}, \tag{65}$$

where $\Delta = \int_0^{s_1} \cos\theta(s)\, ds$ is the axial distance subtended by the end segment. As above, this implies that

$$\sin\left(\frac{\theta_a}{2}\right) = k = \sqrt{\frac{B - \Delta}{2B}}; \qquad B = \sqrt{\Delta^2 + h^2}. \tag{66}$$

We also have the overall displacement constraint

$$d = 1 + 2n(\Delta - s_1). \tag{67}$$

Treating the end segment as the first buckling mode of a pinned-pinned beam of length s_1, from (50) we have

$$\sqrt{\Delta^2 + h^2} = \left[\frac{2E(k)}{K(k)} - 1\right] s_1, \tag{68}$$

and, via (65),

$$\lambda = \frac{\Delta}{\sqrt{\Delta^2 + h^2}}\left[\frac{2K(k)}{s_1}\right]^2; \qquad \mu = \frac{h}{\sqrt{\Delta^2 + h^2}}\left[\frac{2K(k)}{s_1}\right]^2. \tag{69}$$

(Note that the constraint $\int_0^{s_1} \sin\theta(s)\, ds = h$ is satisfied automatically in this formulation.) Given d, h, and n, (66)–(68) may be solved uniquely for s_1 and Δ and the loads λ and μ found from (69). In this way the branch of solutions may be followed (with decreasing s_1) from $s_1 = 1/2n$.

As above, we may use the approximations (52) in (68)–(69) to estimate λ and other quantities such as s_1 in terms of d. After some manipulation, we obtain

$$s_1 \approx \frac{h}{2k(1 - k^2)^{3/2}}, \qquad k \approx \frac{1 - d}{3nh},$$

and

$$\lambda = \frac{4\pi^2}{9n^2h^4}(1-d)^2\left[1 - \frac{(1-d)^2}{2n^2h^2} + \mathcal{O}(|1-d|^4)\right]. \tag{70}$$

Secondary buckling of the central straight segment is governed by (9), with critical load

$$\lambda_n^{sb} = \frac{4\pi^2}{(s_2 - s_1)^2}. \tag{71}$$

Using $s_2 = \frac{1}{n} - s_1$, matching the axial load with (69), and manipulation of (66) and (68) lead to the expressions in (23)–(24).

The Clamped-Pinned Case

We now turn to the clamped-pinned case described by (7) and (12). This problem is reformulated much as the pinned-contact case (8) treated above. Letting $\psi = \theta + \theta_a$, $\tan\theta_a = \frac{\mu}{\lambda}$, (7) becomes

$$\begin{aligned} \psi'' + \tilde{\lambda}\sin\psi = 0; \qquad & \tilde{\lambda} = \sqrt{\lambda^2 + \mu^2}, \\ \psi(0) = \theta_a, \qquad & \psi(1) = 0, \end{aligned} \tag{72}$$

with displacement constraints

$$x(1) = \int_0^1 \cos(\psi - \theta_a)\,ds = \frac{\lambda}{\tilde{\lambda}}\int_0^1 \cos\psi\,ds + \frac{\mu}{\tilde{\lambda}}\int_0^1 \sin\psi\,ds = d, \tag{73}$$

$$y(1) = \int_0^1 \sin(\psi - \theta_a)\,ds = \frac{\lambda}{\tilde{\lambda}}\int_0^1 \sin\psi\,ds - \frac{\mu}{\tilde{\lambda}}\int_0^1 \cos\psi\,ds = 0. \tag{74}$$

From Figure 3(c), for buckling in the n-th mode, we are interested in solutions which make between $2n$ and $2n+1$ quarter-circuits of the origin in the phase plane. Consequently, as above, we deduce from (46) that

$$(2n+1)K(k) - F(\phi_a; k) = \sqrt{\tilde{\lambda}}, \tag{75}$$

and

$$\begin{aligned} \int_0^1 \cos\psi\,ds &= \frac{1}{\sqrt{\tilde{\lambda}}}\{(2n+1)[2E(k) - K(k)] \\ &\quad - [2E(\phi_a; k) - F(\phi_a; k)]\}, \end{aligned} \tag{76}$$

$$\int_0^1 \sin\psi\,ds = \frac{2}{\tilde{\lambda}}\sqrt{\frac{(2k^2-1)\tilde{\lambda} + \lambda}{2}}. \tag{77}$$

These expressions in turn lead to:

$$\lambda d = 2\sqrt{\tilde{\lambda}}[(2n+1)E(k) - E(\phi_a; k)] - \tilde{\lambda}, \tag{78}$$

$$\mu d = 2\sqrt{\frac{(2k^2-1)\tilde{\lambda}+\lambda}{2}}, \tag{79}$$

where $k = \sin(\frac{\psi_0}{2})$ and $\sin\phi_a = \sin(\frac{\theta_a}{2})/\sin(\frac{\psi_0}{2})$, as before.

The condition for first contact is obtained from the relations above by additionally requiring

$$\int_0^{s_1} \sin(\psi - \theta_a)\, ds = \frac{\lambda}{\tilde{\lambda}} \int_0^{s_1} \sin\psi\, ds - \frac{\mu}{\tilde{\lambda}} \int_0^{s_1} \cos\psi\, ds = h, \tag{80}$$

where $s = s_1$ denotes the first extremum $\theta'(s) = 0$. Referring to the phase plane of Figure 3(b), we compute

$$\int_0^{s_1} \cos\psi\, ds = \frac{2}{\sqrt{\tilde{\lambda}}}\{[2E(k) - K(k)] - [2E(\phi_a; k) - F(\phi_a; k)]\}, \tag{81}$$

$$\int_0^{s_1} \sin\psi\, ds = -\frac{4k}{\sqrt{\tilde{\lambda}}}[\cos\phi\,|_{\phi_a}^{\frac{\pi}{2}}] = \frac{4}{\tilde{\lambda}}\sqrt{\frac{(2k^2-1)\tilde{\lambda}+\lambda}{2}}. \tag{82}$$

Substituting from (75) and (78)–(79), (80)–(82) lead to the condition

$$\mu[2E(k) - K(k)] = \frac{\tilde{\lambda}^{\frac{3}{2}} h}{4n}. \tag{83}$$

Equations (27)–(30) are simply (75), (78)–(79), and (83).

When internal moments are zero at the contact point (or throughout the contact region), the resultant of axial and lateral end loads must pass through the boundary points $s = 0, s_1$ and $s = s_2, 1$. We define the geometrical conditions

$$\tan\theta_j = \frac{h}{\Delta_j} = \frac{\mu_j}{\lambda}, \tag{84}$$

where $\Delta_1 = \int_0^{s_1} \cos\theta(s)\, ds$ and $\Delta_2 = \int_{s_2}^1 \cos\theta(s)\, ds$. Assembling the elements of the limiting cases of figures 3(d), (e), and (c) and appealing to the pinned-pinned theory as in (66)–(69), we obtain

$$K(k_1) = \frac{\sqrt{\tilde{\lambda}_1}s_1}{4}; \qquad K(k_2) = \frac{\sqrt{\tilde{\lambda}_2}(1-s_2)}{2}; \tag{85}$$

$$B_1 = \left[\frac{2E(k_1)}{K(k_1)} - 1\right]s_1; \qquad B_2 = \left[\frac{2E(k_2)}{K(k_2)} - 1\right](1-s_2), \tag{86}$$

and

$$k_j = \sqrt{\frac{B_j - \Delta_j}{2B_j}}; \qquad B_j = \sqrt{\Delta_j^2 + h^2}; \qquad \tilde{\lambda}_j = \sqrt{\lambda^2 + \mu_j^2}, \tag{87}$$

for $j = 1, 2$, along with the overall axial displacement constraint,

$$d = \Delta_1 + \Delta_2 + (s_2 - s_1). \tag{88}$$

Note that the clamped-contact element is effectively in the second pinned-pinned mode, and the contact-pinned element in the first. From (84) and (88), we have

$$\tilde{\lambda_j} = \lambda \frac{B_j}{\Delta_j}, \tag{89}$$

and using this and the other definitions of (88), we may regard (85)–(86) and (88) as five equations to be solved simultaneously for the unknown s_j, Δ_j and λ, given d and h.

The two critical loads occur when $s_1 = s_2$ and when

$$\lambda = \frac{4\pi^2}{(s_2 - s_1)^2}, \tag{90}$$

leading to the conditions specified in (31)–(36). Here, as in Section 2.2, we give expressions for only the first mode.

Acknowledgments

This work was supported by OTKA grants T015851 and F021307 and MKM grant 815 (GD), AMFK Grant 483/96, DoE Grant DE-FG02-95ER25238 (PH), and an educational grant from Hercules (BR). Tim Healey introduced us to Feodosyev's work. Ralf Wittenberg coerced Maple into correctly solving some of the elliptic function relations in Section 2. John Maddocks provided several useful comments.

References

[AG90] E. L. Allgower and K. Georg. *Numerical Continuation Methods: An Introduction*. Springer-Verlag, Berlin, 1990.

[Ant95] S. S. Antman. *Nonlinear Problems of Elasticity*. Springer-Verlag, New York, 1995.

[AS65] M. Abramowitz and I. A. Stegun. *Handbook of Mathematical Functions*. Dover Publications, New York, 1965.

[DG95] G. Domokos and Zs. Gáspár. A global, direct algorithm for path-following and active static control of elastic bar structures. *Int. J. Struct. Mach.*, 23 (4):549–571, 1995.

[Dom94] G. Domokos. Global description of elastic bars. *Zeitschr. Angew. Math. Mech.*, 74 (4):T289–T291, 1994.

[Eul44] L. Euler. Additamentum I de curvis elasticis, methodus inveniendi lineas curvas maximi minimivi proprietate gaudentes. In *Opera Omnia I, vol. 24*, 231–197. Bousquet, Lausanne, 1744.

[Feo77] V. I. Feodosyev. *Selected Problems and Questions in Strength of Materials*. Mir, Moscow, 1977. Translated from the Russian by M. Konyaeva.

[KF73] J. B. Keller and J. E. Flaherty. Contact problems involving a buckled elastica. *SIAM J. Appl. Math.*, 24:215–225, 1973.

[KFR72] J. B. Keller, J. E. Flaherty, and S. I. Rubinow. Post buckling behavior of elastic tubes and rings with opposite sides in contact. *SIAM J. Appl. Math.*, 23:446–455, 1972.

[Lov27] A. E. H. Love. *A Treatise on the Mathematical Theory of Elasticity*. Cambridge University Press, Cambridge, UK, 1927. Reprinted by Dover Publications, New York.

[Mad84] J. H. Maddocks. Stability of nonlinearly elastic rods. *Arch. Rat. Mech. Anal.*, 85:311–354, 1984.

[Mad87] J. H. Maddocks. Stability and folds. *Arch. Rat. Mech. Anal.*, 99:301–328, 1987.

[MK95] L. Mahadevan and J. B. Keller. Periodic folding of thin sheets. *SIAM J. Appl. Math.*, 55:1609–1624, 1995.

[Rik79] E. Riks. An incremental approach to the solution of snapping and buckling problems. *Int. J. Solids Struct.*, 15:529–551, 1979.

[Tho65] W. T. Thomson. *Vibration Theory and Applications*. Prentice Hall, New York, 1965.